

Field orientation dependence of magnetization reversal in thin films with perpendicular magnetic anisotropy

Lorenzo Fallarino,^{1,*} Ondrej Hovorka,² and Andreas Berger¹

¹*CIC nanoGUNE, Tolosa Hiribidea 76, 20018 Donostia-San Sebastian, Spain*

²*Faculty of Engineering and the Environment, University of Southampton, Southampton, SO16 7QF, United Kingdom*

(Received 24 August 2015; revised manuscript received 8 June 2016; published 8 August 2016)

The magnetization reversal process of hexagonal-close-packed (hcp) (0001) oriented Co and Co₉₀Ru₁₀ thin films with perpendicular magnetic anisotropy (PMA) has been studied as a function of temperature and applied magnetic field angle. Room temperature pure cobalt exhibits two characteristic reversal mechanisms. For angles near in-plane field orientation, the magnetization reversal proceeds via instability of the uniform magnetic state, whereas in the vicinity of the out-of-plane (OP) orientation, magnetization inversion takes place by means of domain nucleation. Temperature dependent measurements enable the modification of the magnetocrystalline anisotropy and reveal a gradual disappearance of the domain nucleation process during magnetization reversal for elevated temperatures. Ultimately, this suppression of the domain nucleation process leads to the exclusive occurrence of uniform state instability reversal for all field orientations at sufficiently high temperature. Comparative magnetic measurements of Co₉₀Ru₁₀ alloy samples allow the identification and confirmation of the high temperature remanent magnetization state of cobalt as an OP stripe domain state despite the reduction of magnetocrystalline anisotropy. Detailed micromagnetic simulations supplement the experimental results and corroborate the physical understanding of the temperature dependent behavior. Moreover, they enable a comprehensive identification of the complex energy balance in magnetic films with PMA, for which three different magnetic phases occur for sufficiently high anisotropy values, whose coexistence point is tricritical in nature.

DOI: [10.1103/PhysRevB.94.064408](https://doi.org/10.1103/PhysRevB.94.064408)

I. INTRODUCTION

Magnetic thin films with perpendicular magnetic anisotropy (PMA) are an important research subject in the field of ferromagnetism. Interestingly, this is traditionally not related to their relevance in applications, such as hard disk drive technology, where PMA films have had a crucial importance for the progress during the last decades [1,2]. Instead, the prominence of PMA films as a research subject is related to the fact that, in these systems, magnetocrystalline anisotropy and magnetostatic self-interaction are opposing each other. This causes the occurrence of nonuniform microscopic magnetization states as a pathway to minimize the total energy, even in materials such as the stereotypical elemental ferromagnets Fe, Co, Ni, and Gd that otherwise have a simple ferromagnetic ground state [3–6]. Thus, PMA films have been a true test case for our understanding of ferromagnets, and correspondingly, they have defined key achievements toward a complete understanding of ferromagnetism for decades.

In their 1935 landmark paper, Landau and Lifshitz developed domain theory, conceptually introduced by Weiss in 1906 [7], for the purpose of quantitatively describing and predicting the occurrence of nonuniform magnetic regions in ferromagnetic crystals [8], and in the 1940s, Kittel achieved a complete description of the magnetostatic energy for a nonuniform magnetization state in a macroscopic ferromagnet by investigating magnetic films with PMA [9,10]. This solution was later extended by Kooy and Enz [11] to the case in which the sample thickness was comparable to the domain size, enabling a quantitatively accurate description of

nonuniform magnetization reversal based upon a microscopic theory [11]. Subsequently, Muller and Brown derived independently from each other exact analytic solutions of nonuniform magnetization states in macroscopic ferromagnets [12]. In the 1980s and 1990s, PMA films have been instrumental for the experimental discovery and exploration of surface and interface anisotropy, as well as the thickness and temperature-induced reorientation transitions [13–28], hereby addressing fundamental questions about the stability of ferromagnetism in two-dimensional systems, spin-wave instabilities, and the energetics of domain states in ultrathin films [29–34].

All this work has led to an apparently very complete understanding of thin magnetic films with PMA, their micromagnetic states, and magnetization reversal. The majority of these studies, though, either utilize in-plane (IP) or out-of-plane (OP) orientation of the applied magnetic field, but not any intermediate field angles [35–40], since only minor domain structure differences are observed in remanence after applying different field orientations [35]. As a result, thin film PMA ferromagnets, such as Co, were assumed to exhibit rather simple H - β phase diagrams, with β being the angle between the IP orientation and the direction of the magnetic field. This is, however, surprising because the magnetization reversal processes for IP and OP applied fields are qualitatively very different. Indeed, once H is applied along the OP orientation, $\beta = 90^\circ$, magnetization reversal occurs as a first-order phase transition via nucleation, whereas processes consistent with a second-order phase transition are observable in the IP orientation, $\beta = 0^\circ$. For pure Co films, it was recently shown that the two regimes can cross at a certain intermediate β value, and given the different order of the two phase transitions from a uniform to a nonuniform magnetic state, the crossing point was interpreted as a tricritical point [41]. Albeit the

*Corresponding author: l.fallarino@nanogune.eu

existence of complexity for the H - β phase diagram of PMA films was disclosed in that paper, only a single ratio of magnetocrystalline anisotropy to magnetostatic energy was explored, resulting in only a limited view and understanding of the phenomenon. Therefore, the investigation of different energy ratios between the two competing terms that are responsible for the different magnetization reversal paths in PMA films is still an outstanding fundamental problem, without which a complete understanding and rigorous description of the magnetism in PMA thin films cannot be achieved. This paper is the attempt to facilitate this complete understanding of H - β phase diagrams for PMA films.

As described before, magnetocrystalline anisotropy is an important energy term that controls the preferential orientation of the magnetization in materials, as well as the specifics of resulting micromagnetic states via the competition with the magnetostatic energy. In general, magnetocrystalline anisotropy depends on material composition and crystal structure [42–45], and moreover, it exhibits a relevant temperature dependence, which turns out to be very strong for Co, just above room temperature (RT). This is in stark contrast to the saturation magnetization M_s and thus to the magnetostatic energy, which is nearly independent of temperature in this regime [46,47]. This makes Co an attractive material to explore the magnetization reversal and the phase space of PMA films as the energy balance is changed between magnetocrystalline anisotropy energy, characterized by its constant K , and the magnetostatic energy, which is proportional to $(M_s)^2$. This can be easily and very efficiently achieved by varying the temperature for PMA Co films. Alternatively, a tuning of the energy balance can be obtained by alloying Co-based films with different materials [42,48–54]. Furthermore, the possible existence of the already mentioned tricritical point implies the existence of three different thermodynamic phases and their simultaneous criticality at this very point. Therefore, an experimental investigation of the temperature dependent or compositionally controlled H - β phase diagrams, supported by detailed micromagnetic modeling, should allow for a clear identification of the three anticipated magnetic phases for PMA films. At the same time, the modification of the thermodynamic landscape may also possibly lead to the discovery of fundamentally different phase diagrams, including the potential suppression of the energy balance dependent tricritical point.

Following this detailed discussion of prior knowledge on PMA films, the purpose of this paper is (i) to provide a complete exploration and description of the magnetization reversal of PMA films as a function of the energy balance between magnetostatic and anisotropy energies, in contrast to the single energy ratio work done previously [41] and (ii) to verify the existence of the tricritical point in the H - β phase diagram, speculatively introduced in our recent paper [41]. Consequently, we present a detailed study of the structural, magnetic, and magnetization reversal properties of epitaxial Co and $\text{Co}_{90}\text{Ru}_{10}$ thin films grown with (0001) crystallographic orientation, together with detailed micromagnetic modeling to address exactly these questions and goals.

The paper is organized as follows. We describe experimental and simulation specific details in Secs. II A and II B, respectively. Then, in Sec. III A, the identification of the crystal structure and the evaluation of the epitaxial relationship are

shown. In Sec. III B, the RT magnetic characterization is presented and analyzed. In Sec. III C, the composition and temperature dependent experimental results are shown and discussed. Section III D shows micromagnetic simulation results in order to further analyze the entirety of the experimental data. Section IV provides a summary of the accomplished results and general conclusions that can be drawn from our work.

II. METHODS

A. Experimental methods

Co and $\text{Co}_{90}\text{Ru}_{10}$ films of 200 nm thickness were prepared by dc magnetron sputter and cosputter deposition in an ultrahigh vacuum (UHV) deposition system (ATC series from AJA International, Inc.) with a base pressure of better than 3×10^{-6} Pa. Si (111) substrates were first cleaned in organic solvents and washed off in deionized water, then etched with hydrofluoric acid (HF) in order to remove the native SiO_2 prior to the insertion into the UHV sputter system. For each layer, the deposition process was started only after presputtering each of the targets for at least 30 s, using a pressure of 4×10^{-1} Pa of pure Ar atmosphere. As a template for the growth of high quality epitaxial (0001) hexagonal-close-packed (hcp) Co and hcp $\text{Co}_{90}\text{Ru}_{10}$ films, a sequence of 12 nm Ag, 30 nm Ti, and 20 nm Ru was deposited at RT, using plasma power settings of 40, 200, and 30 W, respectively. Thereafter, the Co or CoRu deposition was performed at 573 K, followed by a thermal annealing at the same temperature for 30 min in order to achieve an improved c -axis alignment and correspondingly enhanced magnetic properties [48,55]. The subsequent cooling process of the completed magnetic samples has been carefully carried out at a rate of 5 K min^{-1} down to RT to avoid the formation of the face-centered-cubic (fcc) phase of Co or CoRu. Each sample was then coated with 10 nm of amorphous SiO_2 to avoid surface oxidation and contamination after removal from the vacuum system. A schematic of such a sample, including its specific layer sequence, is shown in Fig. 1 (top part) together with the unit cell of hcp cobalt with the c -axis orientation along the surface normal and its characteristic planar stacking sequence.

The structural analysis of the samples was performed by means of x-ray diffraction (XRD) utilizing a PANalytical X'Pert Pro diffractometer with $\text{Cu-K}\alpha$ radiation. Magnetization measurements were performed using a commercial MicroMag 3900 vibrating sample magnetometer (VSM), equipped with a 360° rotational stage, allowing for an angular precision of better than 1° and a furnace capable of covering the temperature range from RT up to 1073 K with a temperature resolution of better than 1 K. Magnetic domain patterns were measured via magnetic force microscopy (MFM) using a CSI-NanoObserver tool.

B. Micromagnetic simulation

Extensive micromagnetic simulations using the open-source graphics processing unit (GPU) accelerated micromagnetic software mumax³ [56] have been performed to complement our magnetometry and MFM experiments and to gain further insight into the nature of the underlying magnetization reversal and domain pattern formation. Our

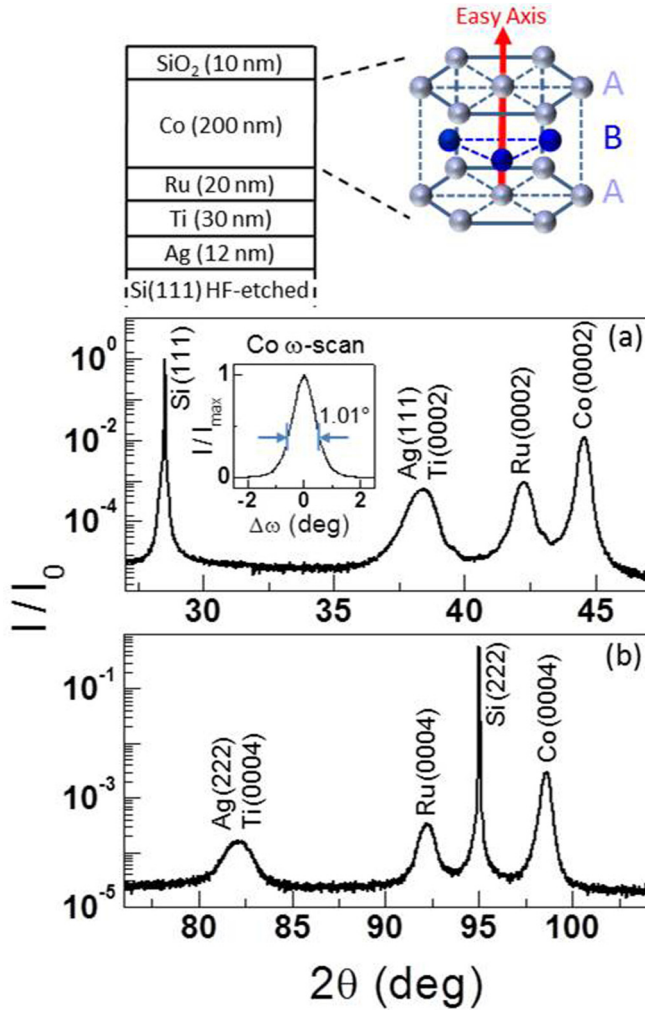


FIG. 1. (a) XRD θ - 2θ pattern showing epitaxial Co (0002), Ru (0002), Ag (111), and Ti (0002) peaks, in addition to the Si (111) substrate signal. The inset shows a rocking curve measurement for the Co (0002) diffraction peak. (b) XRD θ - 2θ pattern showing epitaxial Co (0004), Ru (0004), Ag (222), and Ti (0004) peaks, in addition to the Si (222) substrate signal. The intensity has been normalized in both cases to I_0 , which is the intensity of the (111) Si peak. On top, a schematic of the heteroepitaxial growth sequence is shown for the sample type studied here, including relative thicknesses as well as an illustration of the orientation of the Co c axis with respect to the sample surface plane. The different brightness used for the atoms in the illustration highlights the characteristic stacking sequence of the hcp structure, labeled A-B-A in the figure.

micromagnetic model of the sputter deposited film samples discussed above consists of a simulation unit cell of size $1 \times 1 \mu\text{m}$ in the film plane and 200 nm thickness along the surface normal and utilizes periodic boundary conditions in the plane. The finite difference mesh discretization was chosen to produce $256 \times 256 \times 64$ mesh elements, which for the choice of material constants for Co (saturation magnetization $M_s = 1448 \times 10^3 \text{ A/m}$, and micromagnetic exchange coupling constant $A = 1.5 \times 10^{-11} \text{ J m}^{-1}$ [57]) guaranteed that the discrete mesh feature variation is below the characteristic exchange length in all directions. This specific calculation geometry leads to a mesh resolution that is much finer than the

domain width, while at the same time allowing us to capture numerous domains within our calculated system size.

Two values of the uniaxial anisotropy constant have been considered, $K = 8 \times 10^4 \text{ J m}^{-3}$ and $5.5 \times 10^5 \text{ J m}^{-3}$, which allowed us to mimic the expected behavior at high and low temperatures. To incorporate nonuniformities that are present in any real thin film sample, we included in our modeling random variations of the anisotropy constant around its mean value K , as well as local deviations of the anisotropy axis orientation away from the surface normal, both described by their respective standard deviations σ_K and σ_θ . To implement this local parameter variation, the IP simulation unit cell was divided into 16×16 regions, and randomized anisotropy values and directions were assigned to every region. To reflect the very high quality of crystallographic ordering in the here prepared epitaxial films, the statistical variations were drawn from Gaussian distribution with narrow standard deviations, namely $\sigma_K = 0.5\%$ and $\sigma_\theta = 0.5^\circ$.

The micromagnetic simulations set up in this way have been used to generate two different types of calculations, namely a magnetization state evolution driven by changing the external field amplitude H at a fixed field angle β , i.e. the conventional magnetization reversal process, and a state evolution process driven by changing β at fixed H . The respective calculations were done by varying either H or β in small steps, always starting from positive saturation and relaxing the total energy at every step. The optimum step size was chosen by means of reducing it until the calculated behavior no longer changed upon further reduction.

Finally, at every value of H and β , the corresponding domain pattern was exported and its main features analyzed using image processing techniques, which allowed a classification and analysis of the phase space.

III. RESULTS AND DISCUSSIONS

A. Structural characterization

In order to characterize the crystallographic structure of each layer and to measure the OP crystalline grain dispersion, conventional XRD θ - 2θ scans and rocking curve measurements were performed. In addition, the IP epitaxial relationships between the substrate and the epitaxial layers were studied by means of XRD φ scans at specific crystallographic poles. Figure 1 illustrates XRD θ - 2θ scans in the angular range (a) from 27 to 47° and (b) from 76° to 104° . In (a), the measurement shows four clearly separated Bragg diffraction peaks. They correspond to the Si (111) substrate, Ru (0002), and hcp Co (0002) lattice planes, whereas the slightly broader peak that appears at $2\theta \approx 38.3^\circ$ is the result of the overlapped signals coming from the Ag (111) and Ti (0002) diffraction planes. For larger scattering angles, shown in (b), four interference peaks are observed at the positions of Ru (0004), Si (222) and hcp Co (0004) scattering angles and at $2\theta \approx 82.1^\circ$. This somewhat broadened peak originates from a superposition of the Ag (222) and Ti (0004) Bragg peaks. Beside the substrate peaks, the total angular range shows only well-defined fcc (nnn) and hcp ($000l$) peaks, without the appearance of any other Bragg reflection. Thus, our structural sample analysis verifies the high crystallographic quality of the

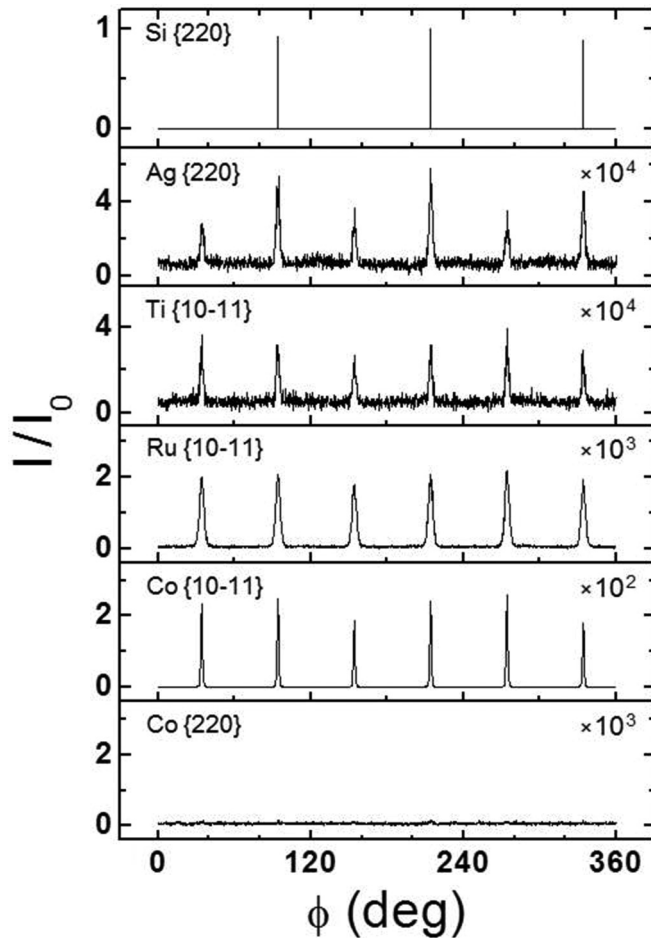


FIG. 2. XRD ϕ scans measured at the Si {220}, Ag {220}, Ti {10-11}, Ru {10-11}, Co {10-11}, and Co {220} poles.

optimized layer growth sequence resulting in well-ordered hcp Co films with perpendicular c -axis orientation that is necessary for a preferential OP orientation of the magnetization, given that the c axis is the easy magnetization axis for Co.

To verify the narrow c -axis dispersion in our samples, rocking curve measurements have been performed for the Co (0002) peak [inset in Fig. 1 (a)]. The full width at half maximum value of the peak is $1.01 \pm 0.01^\circ$, indicating that our Co films achieve excellent alignment of the c -axis orientation normal to the sample surface, if compared to previous papers [41,58–61]. In order to confirm the IP epitaxial alignment of the different layers in our growth sequence, XRD ϕ scan measurements were carried out and are shown in Fig. 2. As expected from the stereographic projection, three diffraction peaks separated by 120° were measured in the Si {220} pole scan, while six evenly spaced peaks were observed from the Ag {220}, which indicates the existence of twinned orientations of the Ag grains [62]. Ti, Ru, and Co, at the {10-11} poles, show all six diffraction peaks, in agreement with the stereographic projection of a single crystal hcp (0001) surface orientation. Also, the Ti, Ru, and Co peaks appear at the correct angles with respect to the Si substrate, thus verifying the epitaxial nature of our samples. Moreover, in order to corroborate the pure hcp crystal nature of our Co thin films,

ϕ scan measurements at the fcc Co {220} pole have been performed. In the entire angular range, no presence of fcc Co could be detected, as indicated by the complete absence of any constructive diffraction peak. Using the background intensity of this measurement to quantify possible fcc concentrations in our films, we have determined that their volume contribution must be less than 0.26% of the total Co film.

The structural characterization of our 200 nm $\text{Co}_{90}\text{Ru}_{10}$ films has been performed via θ - 2θ scans in the $25^\circ \leq 2\theta \leq 110^\circ$ angular range (not shown). Together with the reference substrate peaks and the overlapping Ag and Ti peaks, well-defined hcp Ru, and hcp $\text{Co}_{90}\text{Ru}_{10}$ (0002) and (0004) peaks have been measured that exhibit nearly identical widths if compared to the pattern of the pure cobalt sample, without the appearance of any other crystallographic diffraction peak. The hcp $\text{Co}_{90}\text{Ru}_{10}$ (0002) peak position at $2\theta = 44.33^\circ$ is shifted by 0.23° towards lower diffraction angles in comparison to the measured hcp Co (0002) peak position, which we observe at $2\theta = 44.56^\circ$. This peak shift, in the absence of significant broadening, verifies the simple Co substitution by Ru, corresponding to an increase of the lattice constants by introducing Ru into the hcp lattice. Rocking curve measurements for the $\text{Co}_{90}\text{Ru}_{10}$ (0002) peak reveal a full width at half maximum of $1.34 \pm 0.01^\circ$, slightly larger than that of pure Co, but still indicating the excellent c -axis alignment of our alloy films, especially if compared to previous findings [58–61]. The ϕ scan measurements revealed very good IP epitaxial relationships between the Si substrate and the metal layers, with an upper estimate of less than 0.51% fcc $\text{Co}_{90}\text{Ru}_{10}$ being possibly present in our films. For both sample types, the epitaxial quality and the narrow easy-axis dispersion verify the efficacy of the deposition procedure that we utilized for our work here.

B. RT magnetic characterization

Figure 3 presents the RT magnetic characterization of a 200 nm thick Co (0001) film sample. The top part shows the magnetization curves $M(H)$ measured for an external magnetic field applied perpendicular, Fig. 3(a), and parallel to the film plane, Fig. 3(b). The two curves, well documented in literature [34–38], are almost identical in the high field regime, for $\mu_0 H > \mu_0 H_s \approx \pm 1.5$ T, where the system exhibits a uniform magnetization state parallel to the direction of the applied magnetic field. In the OP configuration, once the field is lowered, the uniform state is altered by the formation of bubblelike domains with opposite magnetization orientation in order to minimize the total magnetostatic energy. This process starts rather abruptly at the nucleation field $\mu_0 H_n \approx 1.3$ T, leading to a drop in the magnetization. As the field is further reduced, the nucleation domain density increases, and their dimensions grow, resulting in the linear field dependence of the magnetization down to $\mu_0 H = 0$ T, where a small hysteresis effect is the result of sample imperfections. In the IP field geometry, Fig. 3(b), the saturated state becomes unstable upon reducing the field strength and undergoes laterally alternating magnetization rotations driven by the PMA, which culminates in the formation of a remanent stripe domain configuration. However, even in remanence, a relevant IP magnetization persists, which was aligned during the field sequence, and

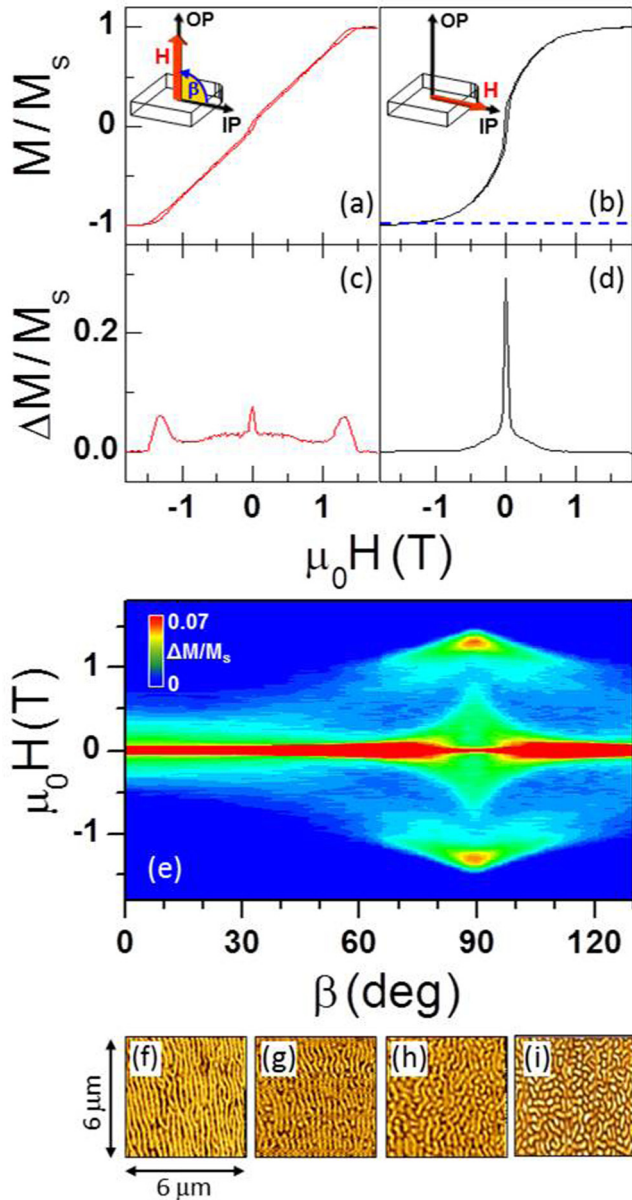


FIG. 3. (a) OP hysteresis loops of a 200 nm thick Co (0001) sample, measured at RT by VSM. (b) IP hysteresis loops measured at RT by VSM; the insets in (a) and (b) display the direction of the magnetic field with respect to the sample surface, which defines the angle β . For both measurements, the diamagnetic background signal coming from the substrate has been subtracted. $\Delta M/M_s$ data for (c) $\beta = 90^\circ$ (c), and for (d) $\beta = 0^\circ$. (e) $\Delta M/M_s(\beta, H)$ (color-coded) map, indicating the hysteretic regions of the magnetic reversal process; the data are normalized to the saturation magnetization M_s . The signal scale (color code) is defined in the figure. RT MFM images, measured on the same Co sample, for remanent magnetic states after reducing the magnetic field from $\mu_0 H = 1.8$ to 0 T applied at angles (f) $\beta = 0^\circ$, (g) $\beta = 40^\circ$, (h) $\beta = 80^\circ$, and (i) $\beta = 90^\circ$.

it is responsible for the hysteresis that occurs for low field values in this field geometry.

Therefore, two fundamentally different magnetization processes take place, as discussed in a previous paper [41]. When the magnetic field is applied perpendicular to the substrate, the

transition from saturated to domain state occurs as a first-order phase transition, mediated by means of domain nucleation. In contrast, the uniform magnetic state becomes unstable upon lowering the magnetic field applied parallel to the sample surface, undergoing a second-order phase transition.

For the purpose of analyzing the magnetization reversal mechanisms and specifically to be able to identify their hysteretic parts, we have adopted a convenient methodology introduced in an earlier paper [41]. This methodology utilizes the normalized difference in magnetization between the two branches of the M vs H loop, namely

$$\frac{\Delta M(\beta, H)}{M_s} = \frac{M_{\text{desc}}(\beta, H) - M_{\text{asc}}(\beta, H)}{M_s}, \quad (1)$$

where $M_{\text{desc}}(\beta, H)$ and $M_{\text{asc}}(\beta, H)$ represent the descending and ascending branches of the magnetization curve for a given magnetic field angle β . Figure 3(c) shows the $\Delta M/M_s$ values vs H for the OP orientation of the applied magnetic field. Here, the small and narrow peak centered at $\mu_0 H = 0$ T corresponds to the low field hysteresis, whereas the two well-pronounced peaks at $\mu_0 H \approx \pm 1.3$ T represent the domain nucleation hysteresis. For the IP case shown in Fig. 3(d), only one sharp peak at $\mu_0 H = 0$ T is present, associated with the hysteretic switching of the remanent IP magnetization component at low fields.

In order to investigate the magnetization reversal processes in the entire field angular range, $M(H)$ curves have been measured for different applied field orientations β between $\beta = 0^\circ$ and $\beta = 130^\circ$, in steps of 5° for $\beta = 0-70^\circ$, and of 2° between $\beta = 70^\circ$ and $\beta = 130^\circ$. The complete angular dependence of the normalized magnetization difference is shown in Fig. 3(e) as a color-coded map of $\Delta M/M_s(\beta, H)$, as defined in Eq. (1). In this plot, the low magnetic field hysteresis forms a central band that extends from left to right over all magnetic field angles, even if it decreases in width near $\beta = 90^\circ$. In contrast, the domain nucleation hysteresis is visible in this plot via two high field “islands” centered at $\mu_0 H = \pm 1.3$ T and $\beta = 90^\circ$. Upon changing β away from the OP orientation, the island width gradually reduces, and they completely disappear for $\beta < 60^\circ$ or $\beta > 120^\circ$. From the results in Fig. 3(e), which corroborate the earlier RT observations in Ref. [41], we can deduce that, in the $\beta < 60^\circ$ and $\beta > 120^\circ$ regimes, the magnetic system is undergoing a second-order rather than a first-order phase transition. In order to confirm the anticipated dependence of the two different reversal behaviors on the remanent magnetic states, MFM measurements were performed as a function of the applied magnetic field angle. As expected, two different types of resulting domain structures have been found: stripe domains for small values of β , Figs. 3(f) and 3(g), and isolated domains produced by nucleation processes, Figs. 3(h) and 3(i), for sufficiently large β . A schematic representation of the two reversal mechanisms, responsible for the different remanent magnetic states imaged by MFM, is shown in Fig. 4. Inset I depicts the instability-driven collectively modulated magnetization structure that resembles a spin-wave state, while inset II displays a schematic of the domain nucleation process, present in our Co film samples for $60^\circ < \beta < 120^\circ$ at RT.

In order to illustrate the origin of the anticipated H - β phase diagram, Fig. 4 shows the orientation dependence for

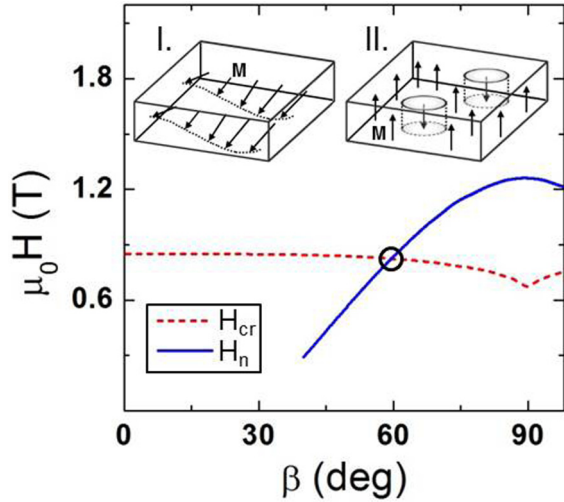


FIG. 4. $H_{cr}(\beta)$ (red) dashed line and $H_n(\beta)$ (blue) line curves calculated for a 200 nm thick film with a PMA field value of $\mu_0 H_k = 1.1$ T [41]. The crossing of $H_{cr}(\beta)$ and $H_n(\beta)$, which defines a tricritical point, is highlighted by a black circle. The inset I shows a schematic of the soft spin-wave mode occurring for low β values, while the inset II displays a schematic of the reversal domain nucleation process occurring for $\beta > 60^\circ$.

the nucleation field H_n (first-order phase transition) as a (blue) solid line and the critical field H_{cr} that describes the stripe-domain instability (second-order phase transition) as a (red) dashed line, reported for such a 200 nm thick Co film in our previous paper [41]. As one can clearly see, H_{cr} shows only a rather weak angular dependence, being nearly constant from 0° up to about 50° , and then slightly decreasing with a minimum at $\beta = 90^\circ$. In contrast, the nucleation field depends strongly on β , with a clear maximum if the field is perpendicular to the sample surface. More importantly, the nucleation field even vanishes for field orientations near $\beta = 40^\circ$ due to the fact that the magnetostatic energy of the saturated state becomes smaller for small β , and a domain nucleation cannot generate a sufficient energy reduction at any positive field value. The different angular dependence of these two processes produces a crossing near $\beta = 60^\circ$ (indicated by a black circle in Fig. 4), which was interpreted to be a tricritical point [41].

Due to the relevance of such a fundamental change in magnetization reversal behavior, it is important to understand and study what defines and governs the existence and position of this tricritical point. In addition, it is of crucial importance to identify and adequately separate the three different magnetic phases to achieve an unambiguous confirmation of the presence of a tricritical point, all of which was not achieved in our previous paper [41]. As already mentioned, one should keep in mind that the underlying phase transitions are both triggered by the competition between magnetostatic energy, which tries to avoid OP magnetization orientations, and the magnetocrystalline anisotropy, which favors OP magnetization orientation in PMA films. Thus, a suitable experimental starting point is the relative variation of these two energy contributions in an otherwise unaltered physical system. This can easily be done for PMA Co films, because Co exhibits a very strong temperature dependence of the magnetocrystalline anisotropy just above RT [46,47], whereas other materials properties,

including the saturation magnetization, and thus the magneto-static energy, vary only minimally in this temperature regime.

C. Temperature and composition dependent magnetic characterization

For the purpose of investigating the relationship between the magnetocrystalline anisotropy K and the nucleation and critical fields, we have utilized the very strong temperature dependence of K in Co and measured $M(H, \beta)$ data for different temperatures, without ever exceeding $T = 573$ K, i.e. the deposition temperature of the magnetic layer [63]. Figure 5 shows $\Delta M/M_s(\beta, H)$ color-coded maps in the $303 \text{ K} \leq T \leq 563 \text{ K}$ temperature range, using temperature

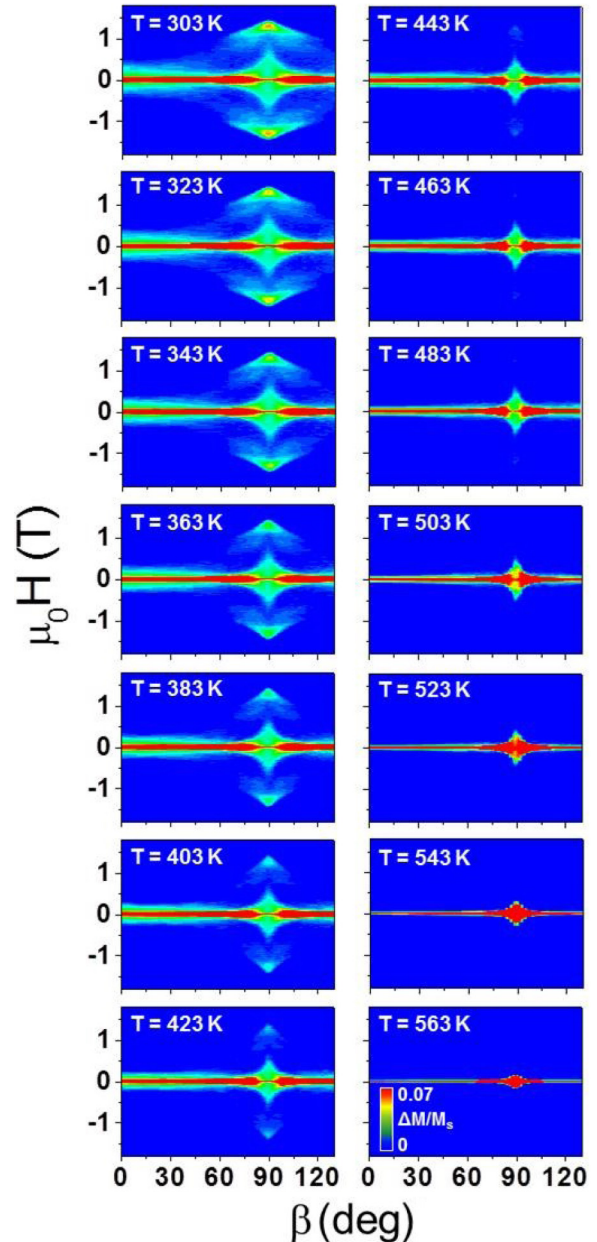


FIG. 5. $\Delta M/M_s$ (color-coded) maps as a function of field angle β and strength $\mu_0 H$ measured for a 200 nm thick epitaxial Co (0001) film at the different temperatures that are indicated in each map. The scale (color code) is defined in the figure.

steps of 20 K. The angular and field resolutions used in these measurements are the same as the ones selected for the RT ones. As can be clearly seen, the resulting $\Delta M/M_s(\beta, H)$ maps strongly depend on temperature, showing significant changes especially in the high magnetic field regime. The most relevant modification involves the two islands near the OP field orientation, which are associated with the nucleation domain hysteresis. Without changing in field position, their angular extension shrinks progressively upon increasing the temperature, up to the point where they collapse entirely. In contrast to this change in the nucleation behavior, the central hysteresis band does not disappear, but instead actually increases significantly between $T = 503$ K and $T = 523$ K near the OP field orientation, before it decreases again for even higher T . Also, it is worthwhile to mention that M_s maintains a nearly constant value in the entire temperature range studied here.

As discussed above, the angular extension of the nucleation islands is controlled by the intersection between the $H_{cr}(\beta)$ and $H_n(\beta)$ curves [41]. Thus, the experimental observations in Fig. 5 reflect the temperature-induced changes in the existence ranges of the two magnetization reversal mechanisms that are triggered by the temperature dependence of the magnetocrystalline anisotropy. In order to visualize this dependence of the reversal mechanism at a certain angle, the same datasets were plotted as $\Delta M/M_s(T, H)$ color-coded maps for different field angles β , displayed in Fig. 6 for four specific β values. For the IP configuration, Fig. 6(a), a gradual reduction of the central hysteretic band with increasing temperature is visible without the appearance of any other hysteretic structure in the entire temperature range. This behavior is fully consistent with the high field hysteresis-free phase transition of an instability-induced stripe domain pattern that leads to a hysteresis peak around zero field due to the existence of a net IP magnetization component for this state. As the temperature increases, this IP magnetization reversal becomes gradually less hysteretic. For the OP geometry, Fig. 6(c), an increase of the temperature corresponds initially to a gradual reduction of the two high field islands, followed by their complete disappearance at $T \approx 430$ K. Conversely, the central band stays nearly constant up to about 500 K, where it starts to expand significantly before it shrinks again at the highest temperatures used in the experiment. If the field is applied along $\beta = 80^\circ$, Fig. 6(b), or $\beta = 100^\circ$, Fig. 6(d), the two nucleation islands appear shifted towards lower fields with respect to the OP geometry, and more relevantly, they vanish at a significantly lower temperature, namely $T \approx 400$ K, while the central hysteretic band exhibits only moderate changes in the entire temperature range. By associating the existence of high field hysteretic behavior with nucleation and the absence of it with instability-driven stripe domain generation, Fig. 6 tells us that the $H_n(\beta)$ and $H_{cr}(\beta)$ curves cross at $\beta = 80^\circ$ for $T = 400$ K, while they cross at significantly smaller β at lower temperature and not at all anymore for $T = 430$ K or higher. In order to exclude the possibility that a temperature-induced reorientation transition with only an IP magnetization at elevated temperature is responsible for the disappearance of the nucleation reversal process, Fig. 7 shows a comparison between the (b) IP and (a) OP magnetization curves $M(H)$ measured at $T = 493$ K for a 200 nm thick Co sample. Hereby, it is important that for

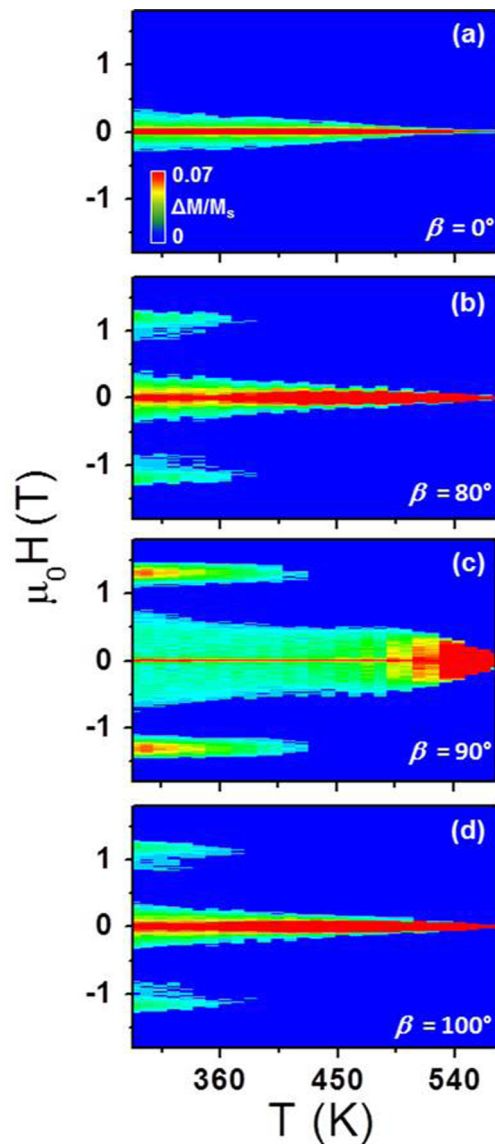


FIG. 6. $\Delta M/M_s$ (color-coded) maps as a function of field strength $\mu_0 H$ and temperature T measured for a 200 nm thick epitaxial Co (0001) film at different values $\beta = 0^\circ, 80^\circ, 90^\circ, 100^\circ$. The scale (color code) is defined in the figure.

the IP configuration, i.e. Fig. 7(b), we find the persistence of a strong curvature of the loop and only a very small remanent magnetization. Thus, the sample is evidently not in an IP magnetization state in remanence, meaning that it must go through a perpendicular domain generation process as one lowers the externally applied field. The absence of high-field hysteresis at $T = 493$ K independent from β thus means that the domain instability process is occurring for all field orientations, while domain nucleation is completely absent.

While a direct confirmation of the high temperature OP remanent domain state via MFM measurements is not accessible to us, the fabricated 200 nm thick hcp $\text{Co}_{90}\text{Ru}_{10}$ (0001) alloy thin film exhibits a RT magnetic behavior that mimics the high temperature Co film properties very well. Figures 7(c) and 7(d) show RT $M(H)$ curves for this alloy

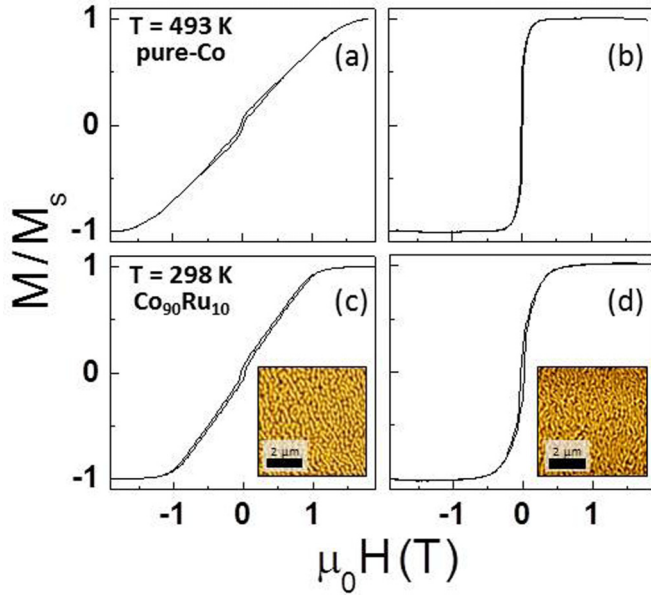


FIG. 7. (a) OP and (b) IP hysteresis loops measured by VSM at $T = 493$ K for a 200 nm thick epitaxial Co (0001) film. (c) OP and (d) IP hysteresis loops measured by VSM at RT for a 200 nm thick epitaxial $\text{Co}_{90}\text{Ru}_{10}$ (0001) film; the insets in (c) and (d) display RT MFM images measured in remanence by first reducing the magnetic field from $\mu_0 H = 1.8$ to 0 T at a fixed angles of (c) $\beta = 90^\circ$ and (d) $\beta = 0^\circ$ for the same $\text{Co}_{90}\text{Ru}_{10}$ alloy sample.

sample in direct comparison with the data for the pure Co film measured at 493 K. As we can see, the IP curve for the alloy film, Fig. 7(d), shows a small central hysteresis, a strong curvature, and only a small remanent magnetic moment. The OP data for this sample, Fig. 7(c), also show very comparable results to the high temperature Co film, including the absence of high field nucleation hysteresis near saturation. The remanent magnetic domain structures connected to the two measured magnetization reversals have been investigated via MFM measurements. First, the $\text{Co}_{90}\text{Ru}_{10}$ sample has been brought to saturation, applying an external magnetic field with a magnitude of $\mu_0 H = 1.8$ T; then the field has been removed, reducing its amplitude in steps of 1000 Oe down to $\mu_0 H = 0$ T. Both images, shown as insets in Figs. 7(c) and 7(d), have then been recorded in the absence of any external magnetic field. Although a meager deterioration of the striplike pattern configuration compared to the pure Co film case is visible, most likely attributable to the slightly worse quality of the alloy sample, both geometries show that the tendency to form a striplike pattern is certainly not reduced upon going from near IP, Fig. 7(d), to near OP field orientation, Fig. 7(c), even if the stripe alignment force of the IP field component is reduced. In addition, our MFM measurements confirm that the system still develops a perpendicular stripe domain state at remanence, even if no nucleation takes place, which can only occur if the OP orientation of the magnetization is preferred.

Utilizing this strong link between the magnetization reversal processes for pure Co at high temperature and the RT $\text{Co}_{90}\text{Ru}_{10}$ alloy behavior, we have confirmed our assumption that there is a temperature range in which Co has perpendicular stripe domains without undergoing domain nucleation

processes, even for the OP field orientation. Moreover, this means that, upon sufficiently lowering the magnetocrystalline anisotropy, an angular independent reversal process is achievable by either heating or by alloying.

D. Micromagnetic simulation results

In order to further confirm the validity of the physical picture deduced from our experimental data, micromagnetic simulations of the field-induced reversal processes have been performed. First, we illustrate excellent agreement between the various calculated and measured magnetization curves, which establishes the credibility of the micromagnetic model. This allows us to then use the model to study the domain pattern formation in different experimentally relevant scenarios. Finally, we define the relevant order parameter here and use it to calculate the field angle dependent phase diagram for Co films with perpendicular anisotropy.

1. Magnetization loops

In Fig. 8, simulated magnetization curves for $K = 5.5 \times 10^5 \text{ J m}^{-3}$ are visualized as (black) thick solid lines, for (b) the IP and (a) the OP field orientations together with the respective experimental data, shown as (red) thin solid lines [64]. Exhibiting an excellent level of similarity with our experimental results, the simulation in Fig. 8(b) shows that the IP magnetization becomes unstable upon lowering the magnetic field from saturation, leading to a transition into a nonuniform magnetization state without the occurrence of any hysteresis. Only at very low field values, we observe hysteretic behavior that is associated with the reversal of the weak remanent IP magnetization component. When the field is applied perpendicular to the sample surface, Fig. 8(a), the

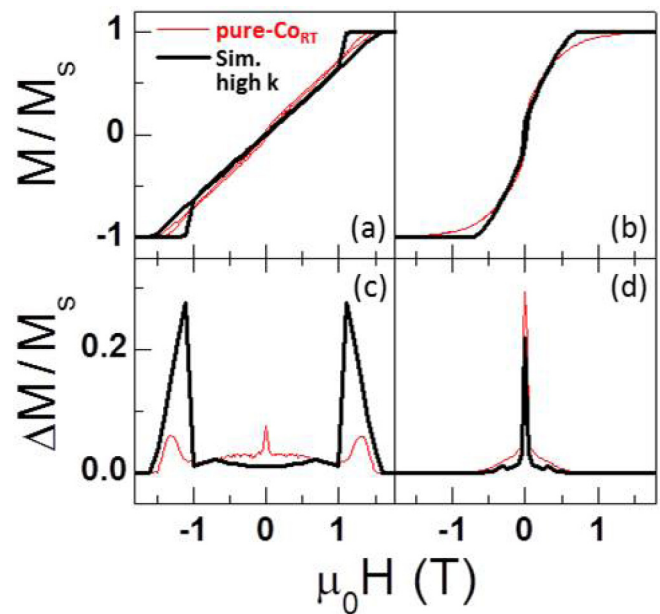


FIG. 8. Hysteresis loops for a 200 nm thick epitaxial Co (0001) film: experimental data are shown as a (red) thin solid line, while simulation results are displayed as (black) thick solid line; (a) shows the OP and (b) the IP behavior. The corresponding $\Delta M/M_s$ curves are shown in (c) for the OP and in (d) for the IP cases.

simulated $M(H)$ data show that the originally saturated state changes its magnetization rather suddenly at the nucleation field. In panels (c) and (d) of Fig. 8, the corresponding values for $\Delta M/M_s$ vs H are displayed in direct comparison with the experiments. For the IP case, Fig. 8(d), only the narrow central peak of IP magnetization reversal near remanence is visible, and its height and position are very well reproduced by the simulation. For the OP case, Fig. 8(c), the calculated curve exhibits hysteresis only at high fields, where the local formation and annihilation of individual up or down domains occurs. While reproducing the positions of the experimental high field peaks very accurately, the peaks resulting from our numerical simulations are enhanced with respect to the experimental case. Also, our calculations do not show the small peak at low fields, which we find experimentally and which is associated with the limited mobility of the domain walls in our samples. These quantitative differences in both field orientations can be explained by an imperfect representation of structural disorder, e.g. defects of the crystal lattice and grain structure, as well as the lack of thermal activation, which is present only in the experimental system. While our micromagnetic simulations allowed us to mimic the temperature dependence of the material parameters, it did not contain actual thermal fluctuations. Therefore, hysteresis effects associated with first-order phase transitions are overemphasized for $T > 0$ K, which explains that the $\Delta M/M_s$ values near the domain nucleation field are significantly larger in the simulation than in the experiment, in which thermal fluctuations are present. Overall, however, the simulation successfully reproduces all key features, namely OP nucleation and IP low field hysteresis and, thus, is in very good qualitative agreement with the experimental data, hereby verifying the fundamental differences between the IP and OP magnetization reversal processes.

In order to confirm the entire field orientation dependence, Fig. 9(c) shows simulated $\Delta M/M_s(\beta, H)$ results for $K = 5.5 \times 10^5 \text{ J m}^{-3}$ as color-coded map. The low magnetic field hysteresis is clearly visible at low β , while it is absent in the proximity of $\beta = 90^\circ$. The two high field islands, representing the domain nucleation hysteresis, are centered at $\beta = 90^\circ$. They reduce gradually upon shifting β away from the OP orientation, and they disappear for $\beta < 60^\circ$. Thus, the calculated map in Fig. 9(c) reproduces all key features of the experimental RT data, plotted in direct comparison in Fig. 9(a), with good quantitative agreement in terms of the magnetic field amplitude and angular range, in which the different hysteretic structures are visible. Only the absolute scale of the $\Delta M/M_s(\beta, H)$ values show significant differences, especially for the two high field islands, which is primarily due to the absence of thermal fluctuations in our calculations, as was already discussed in conjunction with Fig. 8. To explore the behavior of Co films at high temperatures, micromagnetic simulations of the field-induced reversal have been also performed for a smaller anisotropy value, namely $K = 8 \times 10^4 \text{ J m}^{-3}$, without changing any of the other magnetic parameters. Figure 9(d) shows the $\Delta M/M_s(\beta, H)$ color-coded map generated by our simulations in this case. In the entire angular range, only the low field hysteresis band is present, exhibiting its largest ΔM values in the proximity of $\beta = 0$. Upon changing β , the hysteresis band stays fairly constant up to the proximity

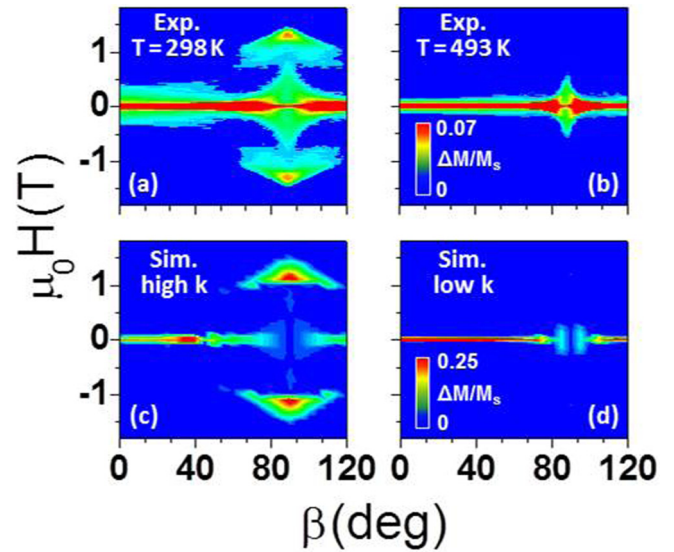


FIG. 9. $\Delta M/M_s$ maps as a function of field angle β and strength $\mu_0 H$ measured for a 200 nm thick epitaxial Co (0001) film at (a) $T = 298$ K and (b) $T = 493$ K. Calculated $\Delta M/M_s(\beta, H)$ maps for a 200 nm thick Co film assuming (c) $K = 5.5 \times 10^5 \text{ J m}^{-3}$ and (d) $K = 8.0 \times 10^4 \text{ J m}^{-3}$. The scales (color code) are defined in the figure.

of $\beta \approx 90^\circ$, where it first increases its field extension and subsequently disappears along the OP field orientation. Just as in the high temperature experimental regime for our Co films, which is displayed in Fig. 9(b) for the purpose of comparison, there are no high field nucleation islands, meaning that, in the entire angular range, the reversal process proceeds via the instability of the uniform magnetic state.

2. Characteristic domain patterns

Figure 9 clearly illustrates that qualitatively different behaviors can emerge depending on the value of anisotropy K , which we managed to tune in our Co films by means of temperature or alloying. For K values that are relatively low, but still sufficiently large to support a stripe domain state in remanence, a case we obtained experimentally at $T = 493$ K in our Co films (the right column plots), the nucleation type hysteresis is absent in contrast to the high K case (the left column plots). The absence of the nucleation phase at low K is confirmed in the entire H - β parameter space upon analyzing the micromagnetic domain pattern, as illustrated in Fig. 10(a). For this, domain patterns were evaluated along the hysteresis loop branch that starts from positive saturation for all orientation angles β . In the calculated domain pattern, shown in Figs. 10(a) and 10(b), the dark and bright regions correspond to the OP magnetization component being up or down, and the intermediate grayscale indicates IP alignment. In both figures, the film sample is uniformly magnetized for all values of β if the applied magnetic field H is sufficiently strong. Reducing H gradually leads to the appearance of the stripe domain pattern in Fig. 10(a) for all values of the field angle β . Thus, there exists only a single type of phase boundary, shown as a dashed (purple) line, which is due to the instability of the uniform state and which triggers a second-order phase transition into a

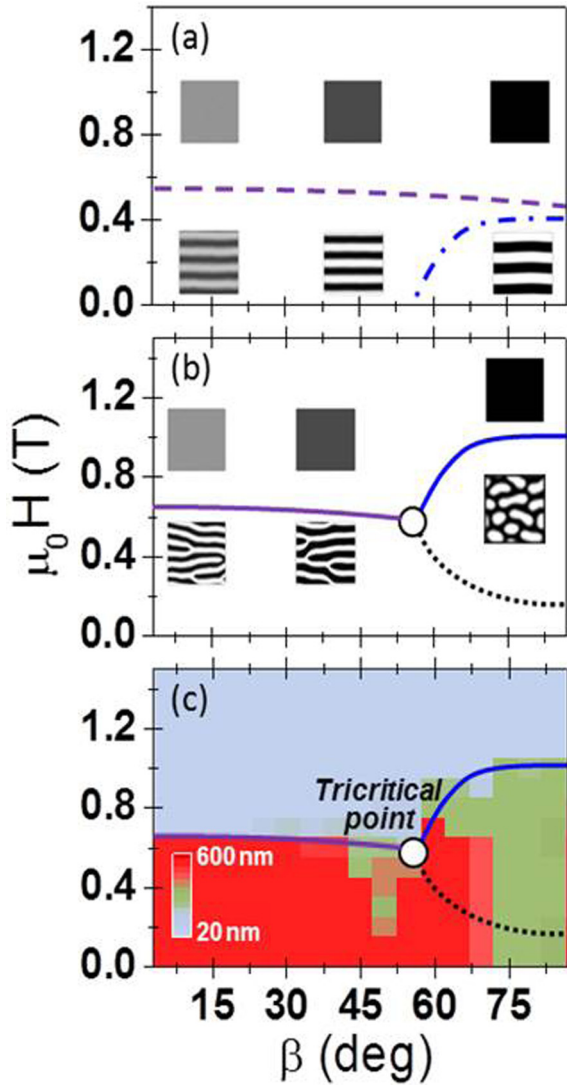


FIG. 10. (a) Calculated phase diagram for a 200 nm thick Co film assuming $K = 8.0 \times 10^4 \text{ J m}^{-3}$. (b) Calculated phase diagram for a 200 nm thick Co film assuming $K = 5.5 \times 10^5 \text{ J m}^{-3}$. The insets in (a) and (b) show simulated domain pattern, with an area of $1 \times 1 \mu\text{m}$, at different field strengths and angles, both corresponding to the position of the inset frame center in each case. (c) Map (color-coded) of the H and β dependence of the order parameter Op for $K = 5.5 \times 10^5 \text{ J m}^{-3}$ that identifies three different phases, their transition lines, and the tricritical point connecting them. The corresponding Op scale bar (color code) is displayed in the figure.

stripe domain state for all β . The onset of nucleation could still result in a positive nucleation field for β values near the OP field orientation, which is indicated by the dashed-dotted (blue) line in Fig. 10(a), but this transition never occurs because the system has already undergone the instability transition prior to reaching field values, where nucleation would be feasible. Thus, the first-order phase transition into a nucleation domain state is suppressed here. It is worthwhile to mention that the dashed line in panel (a) has been generated by examining the evolution of the simulated domain patterns, whereas the dashed-dotted line has been derived from a theoretical model calculation according to [41].

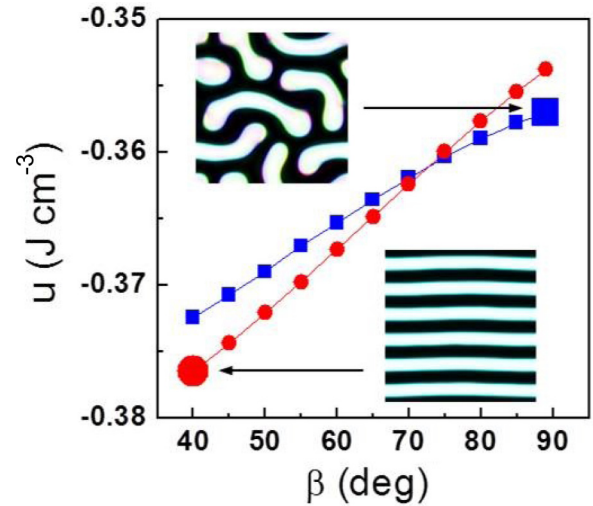


FIG. 11. Applied field angle β dependence of the energy density at an applied field strength of $\mu_0 H = 0.1 \text{ T}$ for two different initial magnetization reversal states, namely: (i) shown as (red) dots, energy values for a stripe domain state that was initially generated via field reduction from saturation at constant $\beta = 40^\circ$ and (ii) shown as (blue) squares, energy values for a nucleation domain state produced initially via field reduction from saturation at $\beta = 89^\circ$. The two insets show the simulated starting pattern for the two different domain states, which are found to change only minimally in the entire β range shown here. The area of the domain pattern is $1 \times 1 \mu\text{m}$.

The behavior is very different and more complex when K is large, i.e. the low temperature case for our Co films, as shown in Fig. 10(b). While the behavior for low β values is fundamentally unchanged, the behavior is substantially altered for sufficiently large β because nucleation occurs at higher field values than the stripe domain instability. Thus, the nature of the phase transition changes upon increasing β from a second-order phase transition near IP orientations to a first-order phase transition near the OP field alignment. Together with this change in the nature of the phase transition occurs a change in the domain type that is found, as can be seen in Fig. 10(b). While the low β domain state consists of system size stripe domains that represent a collective magnetization state, at intermediate field strengths and large β , the magnetization structure is characterized by localized reversal domains that change in density and form, but have a lateral extension far smaller than the system size. This difference in the domain state nature also means that there must be a third phase line that separates the stripe domain states from the nucleation domain states for intermediate field strength. This phase line is also displayed in Fig. 10(b) as a dotted (black) line, together with the tricritical point that join all three phase lines, represented by a circle. The nature of the low field phase line and the fact that it does not extend all the way to $H = 0$ will be discussed in conjunction with Fig. 11 [65].

3. Order parameter and phase diagram

For the purpose of corroborating the qualitative discussion of Figs. 10(a) and 10(b) given above, we have performed a quantitative analysis of the underlying order parameter that allows for a formal distinction of the various phases. This first

requires the definition of an order parameter that is capable of capturing the qualitative change of the domain structure from the approximately circular shape of nucleation domains to the elongated shape of stripe domains. In order to achieve sufficient insensitivity to inhomogeneities and the apparent irregular shapes of magnetized regions within the domain patterns [see Fig. 10(b)], we defined the order parameter $Op(H, \beta)$ for any domain pattern corresponding to a specific pair of H and β as:

$$Op(H, \beta) = \langle r_{g,i} \rangle_{H, \beta} = \frac{1}{N_{\text{sub}}} \sum_{i=1}^{N_{\text{sub}}} r_{g,i} \Big|_{H, \beta}, \quad (2)$$

where N_{sub} is the number of individual disconnected magnetic subdomain regions i with the magnetic moment pointing down (i.e. subregions with $m_z < 0$) that are present within the overall pattern at any positive magnetic field value H . Hereby, $r_{g,i}$ is the radius of gyration for subregion i . The $r_{g,i}$ values are calculated in a standard way by discretizing the area of a subdomain i into n subsections at positions \vec{r}_j and evaluating the sum

$$r_{g,i}^2 = \frac{1}{2n^2} \sum_{k,l}^{n,n} (\vec{r}_k - \vec{r}_l)^2. \quad (3)$$

The order parameter defined in this way vanishes in the presence of a uniform magnetization state, is small but not vanishing for isolated nucleation domains, and exhibits values of the order of the system size for the stripe domain phase. The resulting color-coded $Op(H, \beta)$ map for the high K value of $5.5 \times 10^5 \text{ J m}^{-3}$, corresponding to Fig. 10(b), is shown in Fig. 10(c). Here, the three phases appear as clearly distinct regions corresponding to clearly different order parameter values, which allow a localization of the individual phase boundaries and a confirmation of the qualitative discussion that was presented above in conjunction with Fig. 10(b). A certain level of noise in the region of the tricritical point, noticeable between $\beta = 45$ and 50° , is apparent and is generally expected as a result of the phase coexistence and the extremely flat energy landscape. The standard physical picture is that the nature of the tricritical point leads to a higher multiplicity of state space trajectories that are available within a micromagnetic system, and consequently, it leads to increased fluctuationlike order parameter variations. In our simulations, these ‘‘fluctuations’’ could be averaged out by increasing the system size or averaging over an increased number of simulations with different microscopic realizations of the anisotropy distribution. In addition to this, another aspect of Fig. 10(c) deserves attention because the low field phase line we have drawn schematically on top of the order parameter plot deviates from the actual Op values in the vicinity of $H = 0$. Specifically the, Op values seem to indicate that this phase line intersects with the $H = 0$ axis. Fundamentally, however, this intersection of the phase line does not make any sense because, for $H = 0$, i.e. in the absence of any applied field, all β values on the $H = 0$ axis represent only a single phase space point, given that β is the field orientation axis. Thus, along the $H = 0$ axis, there ought to be only one magnetization state that represents the actual minimum of the free energy. Correspondingly, the low field phase line cannot extend all the way to $H = 0$ and cannot cross the $H = 0$ line.

Instead, it ought to intercept the $\beta = 90^\circ$ axis at a nonvanishing $\mu_0 H$ value. The discrepancy between this phase line and the calculated Op data can be explained if the low field phase line would represent a first-order phase transition. In this case, the nucleation domains would remain a metastable magnetic state for very low $\mu_0 H$ values in the vicinity of $\beta = 90^\circ$, and the lack of thermal excitation in our simulations simply would not allow for the transition to a stripe domain state to occur in this regime. Correspondingly, the phase line could not be exactly positioned by means of our order parameter calculations.

4. Nature of the low field phase boundary

To check this point and to advance our understanding further, we have studied the nature of the phase line separating the stripe and nucleation domains in the low field region [dashed line in Figs. 10(b) and 10(c)]. For this, Fig. 11 shows micromagnetic calculations of the domain state energy density across this phase boundary as a function of the field orientation β at a fixed $\mu_0 H$, upon starting the β variation from two different initial states associated with the respective stripe and nucleation domain phase regions. In particular, the (red) dot symbols in Fig. 11 have been calculated by first reducing the magnetic field from $\mu_0 H = 1.5$ to 0.1 T at a fixed angle of $\beta = 40^\circ$, which produces a stripe domain state [see Figs. 10(b) or 10(c)], upon which the field orientation is changed by increasing β stepwise all the way to 89° . On the other hand, the data represented by (blue) squares are generated by first reducing the magnetic field from $\mu_0 H = 1.5$ to 0.1 T at a fixed angle of $\beta = 89^\circ$, which produces a nucleation domain state, upon which the field orientation is changed by decreasing β stepwise all the way down to 40° . These calculations now enable us to identify the type of phase transition that is given by the low field phase line. First, Fig. 11 demonstrates that two stable solutions with distinct energies persist in the entire β range that is investigated here. Also, the inspection of the domain states verifies that the nature of each individual state remains intact, meaning that all (red) dots and all (blue) squares in Fig. 11 correspond to stripe domain and nucleation domain states, respectively. Furthermore, we can see that the energy levels of these two states cross each other, with the stripe domain state being the lowest energy state for small β , while for β near 90° , the nucleation domain state has lower energy. For $\mu_0 H = 0.1$ T, the crossing occurs at $\beta = 73^\circ$. The existence of multiple (meta-)stable solutions that cross in energy at a specific point verifies the fact that the low field phase line in Figs. 10(b) and 10(c) is indeed a first-order phase transition line, which also explains the slight disagreement between the schematic phase boundary location and the OP data. With the results in Fig. 11, we have now managed to identify the nature of all the phase lines in Figs. 10(b) and 10(c), hereby achieving a detailed understanding of the field orientation dependence of the magnetization reversal in Co films with PMA as well as the qualitative changes that occur upon temperature variation.

IV. CONCLUSIONS

In this paper, we have successfully fabricated epitaxial Co (0001) and $\text{Co}_{90}\text{Ru}_{10}$ (0001) thin films with a mag-

netic easy axis perpendicular to the film plane, very small c -axis dispersion, and an almost complete absence of the fcc phase. The RT measurements of our pure Co films reveal the presence of two very different magnetization reversal processes depending on the applied field angle β , namely an instability-driven process leading to the generation of stripe domains for β values near IP field orientation and a nucleation domain process near OP field orientation that is hysteretic in nature. Our temperature dependent study shows a gradual shrinking of the nucleation regime, so that at sufficiently high temperatures, only the instability-driven second-order phase transition occurs for all angles β . The disappearance of the nucleation regime is driven by the strong temperature dependence of the magnetocrystalline anisotropy and occurs before the anisotropy becomes too weak to support a stripe domain state altogether, i.e. it occurs while stripe domain instability is still dominating the magnetization reversal process. We observe the same type of results when we reduce the magnetocrystalline anisotropy by means of alloying Co with Ru. This type of alloy sample even allows the experimental verification of the stripe domain phase by means of MFM observations for samples, for which the nucleation domain process is already suppressed. Without taking into consideration the specific nature on the magnetocrystalline anisotropy of Co [66], micromagnetic simulations successfully reproduce the RT and high temperature magnetization reversal processes as a function of the applied field angle. Furthermore, by introducing a suitable order parameter based upon the different domain geometries associated with the different domain reversal processes, we have found the H - β phase diagram of RT PMA Co films to contain three different

magnetic phases. We were also able to precisely identify the nature of all the phase lines, allowing us to unambiguously define the crossing point between $H_n(\beta)$ and $H_{cr}(\beta)$ curves as a tricritical point. This has permitted the derivation of a complete phase diagram for a perpendicular magnetic film in an applied field of any orientation and with the full incorporation of the magnetostatic energy term, which leads to a nontrivial modification of the magnetic phases. Given the generality of our observations and the simple assumptions made for the micromagnetic simulations, we expect that our findings will extend to many different ferromagnetic materials that exhibit OP magnetocrystalline anisotropies. Therefore, we consider our paper to be another illustration of substantial relevance of PMA thin films, which enable a very detailed understanding of macroscopic ferromagnets and ferromagnetic phases, a fact that makes them a crucially important test object and leads to an ever more complete and sophisticated understanding of fundamental magnetism.

ACKNOWLEDGMENTS

We acknowledge support from the Basque Government under Project No. PI2015-1-19 and from the Spanish Ministry of Economy and Competitiveness (MINECO/FEDER) under Project No. FIS2015-64519-R. L.F. thanks the Basque Government for the Ph.D. fellowship (Grants No. PRE_2013_1_974, No. PRE_2014_2_142, and No. PRE_2015_2_0126). O.H. gratefully acknowledges fruitful discussions with H. Fangohr, M. Albert, and A. Vansteenkiste.

-
- [1] W. Cain, A. Payne, M. Baldwinson, and R. Hempstead, *IEEE Trans. Magn.* **32**, 97 (1996).
 - [2] S. N. Piramanayagam, *J. Appl. Phys.* **102**, 011301 (2007).
 - [3] T. Garel and S. Doniach, *Phys. Rev. B* **26**, 325 (1982).
 - [4] D. J. Singh, *Phys. Rev. B* **44**, 7451 (1991).
 - [5] R. Allenspach, *J. Magn. Magn. Mat.* **129**, 160 (1994).
 - [6] K. De'Bell, A. B. MacIsaac, and J. P. Whitehead, *Rev. Mod. Phys.* **72**, 225 (2000).
 - [7] P. Weiss, *Comptes Rendus* **143**, 1136 (1906).
 - [8] L. Landau and E. Lifshitz, *Phys. Z. Sowjetunion* **8**, 153 (1935).
 - [9] C. Kittel, *Phys. Rev.* **70**, 965 (1946).
 - [10] C. Kittel, *Rev. Mod. Phys.* **21**, 541 (1949).
 - [11] C. Kooy and U. Enz, *Philips Res. Rep.* **15**, 7 (1960).
 - [12] M. W. Muller, *Phys. Rev.* **122**, 1485 (1961); W. F. Brown, Jr., *ibid.* **124**, 1348 (1961).
 - [13] P. J. Grundy, D. C. Hothersall, G. A. Jones, B. K. Middleton, and R. S. Tebble, *Phys. Status Solidi(a)* **9**, 79 (1972).
 - [14] C. Chappert, K. L. Dang, P. Beauvillain, H. Hurdequint, and D. Renard, *Phys. Rev. B* **34**, 3192 (1986).
 - [15] D. Pescia, M. Stampanoni, G. L. Bona, A. Vaterlaus, R. F. Willis, and F. Meier, *Phys. Rev. Lett.* **58**, 2126 (1987).
 - [16] C. Liu, E. R. Moog, and S. D. Bader, *Phys. Rev. Lett.* **60**, 2422 (1988).
 - [17] T. Beier, H. Jahrreiss, D. Pescia, Th. Woike, and W. Gudat, *Phys. Rev. Lett.* **61**, 1875 (1988).
 - [18] R. Allenspach, M. Stampanoni, and A. Bischof, *Phys. Rev. Lett.* **65**, 3344 (1990).
 - [19] R. Allenspach and A. Bischof, *Phys. Rev. Lett.* **69**, 3385 (1992).
 - [20] B. Schulz and K. Baberschke, *Phys. Rev. B* **50**, 13467 (1994).
 - [21] A. Berger, A. W. Pang, and H. Hopster, *J. Magn. Mag. Mater.* **137**, L1 (1994).
 - [22] A. Berger, A.W. Pang, and H. Hopster, *Phys. Rev. B* **52**, 1078 (1995).
 - [23] A. Berger and H. Hopster, *J. Appl. Phys.* **79**, 5619 (1996).
 - [24] D. M. Donnet, K. M. Krishnan, and A. Yajima, *J. Phys. D* **28**, 1942 (1996).
 - [25] A. Berger and H. Hopster, *Phys. Rev. Lett.* **76**, 519 (1996).
 - [26] J. F. Gregg, W. Allen, K. Ounadjela, M. Viret, M. Hehn, S. M. Thompson, and J. M. D. Coey, *Phys. Rev. Lett.* **77**, 1580 (1996).
 - [27] M. Hehn, K. Ounadjela, R. Ferré, W. Grange, and F. Rousseaux, *Appl. Phys. Lett.* **71**, 2833 (1997).
 - [28] J. U. Thiele, L. Folks, M. F. Toney, and D. K. Weller, *J. Appl. Phys.* **84**, 5686 (1998).
 - [29] R. L. Stamps and B. Hillebrands, *Phys. Rev. B* **43**, 3532 (1991).
 - [30] O. Portmann, A. Vaterlaus, and D. Pescia, *Nature* **422**, 701 (2003).
 - [31] G. Leaf, H. Kaper, M. Yan, V. Novosad, P. Vavassori, R. E. Camley, and M. Grimsditch, *Phys. Rev. Lett.* **96**, 017201 (2006).

- [32] P. Landeros, R. E. Arias, and D. L. Mills, *Phys. Rev. B* **77**, 214405 (2008).
- [33] J. Brandenburg, R. Hühne, L. Schultz, and V. Neu, *Phys. Rev. B* **79**, 054429 (2009).
- [34] N. Saratz, A. Lichtenberger, O. Portmann, U. Ramsperger, A. Vindigni, and D. Pescia, *Phys. Rev. Lett.* **104**, 077203 (2010).
- [35] M. Hehn, S. Padovani, K. Ounadjela, and J. P. Bucher, *Phys. Rev. B* **54**, 3428 (1996).
- [36] M. Hehn, K. Cherifi-Khodjaoui, K. Ounadjela, J. P. Bucher, and J. Arabski, *J. Magn. Magn. Mater.* **165**, 520 (1997).
- [37] M. Kisielewski, A. Maziewski, and V. Zablotski, *J. Magn. Magn. Mater.* **316**, 277 (2007).
- [38] O. Donzelli, M. Bassani, F. Spizzo, and D. Palmeri, *J. Magn. Magn. Mater.* **320**, e261 (2008).
- [39] N. Berggaard, J. P. Jamet, A. Mougin, J. Ferré, J. Gierak, E. Bourhis, and R. Stamps, *Phys. Rev. B* **86**, 094431 (2012).
- [40] J. Gao, S. Tang, Y. Li, W. Xia, T. Tang, and Y. Du, *J. Appl. Phys.* **112**, 073913 (2012).
- [41] A. K. Suszka, A. Etxebarria, O. Idigoras, D. Cortés-Ortuño, P. Landeros, and A. Berger, *Appl. Phys. Lett.* **105**, 222402 (2014).
- [42] N. Inaba, M. Futamoto, and A. Nakamura, *IEEE Trans. Magn.* **34**, 1558 (1998).
- [43] O. Kitakami, N. Kikuchi, S. Okamoto, Y. Shimada, K. Oikawa, Y. Otani, and K. Fukamichi, *J. Magn. Magn. Mat.* **202**, 305 (1999).
- [44] I. Zana, G. Zangari, and M. Shamsuzzoha, *J. Magn. Magn. Mat.* **292**, 266 (2005).
- [45] T. Shimatsu, H. Sato, Y. Okazaki, H. Aoi, H. Muraoka, Y. Nakamura, S. Okamoto, and O. Kitakami, *J. Appl. Phys.* **99**, 08G908 (2006).
- [46] D. M. Paige, B. Szpunar, and B. K. Tanner, *J. Magn. Magn. Mater.* **44**, 239 (1984).
- [47] W. Yang, D. N. Lambeth, and D. E. Laughlin, *J. Appl. Phys.* **87**, 6884 (2000).
- [48] I. S. Lee, H. Rhu, H. J. Lee, and T. D. Lee, *J. Appl. Phys.* **85**, 6133 (1999).
- [49] D. Weller, H. Brändle, G. Gorman, C. J. Lin, and H. Notarys, *Appl. Phys. Lett.* **61**, 2726 (1992).
- [50] O. Idigoras, U. Palomares, A. K. Suszka, L. Fallarino, and A. Berger, *Appl. Phys. Lett.* **103**, 102410 (2013).
- [51] N. Inaba, Y. Uesaka, and M. Futamoto, *IEEE Trans. Magn.* **36**, 54 (2000).
- [52] S. Honda, K. Takahashi, and T. Kusuda, *Jpn. J. Appl. Phys.* **26**, L593 (1987).
- [53] S. Okamoto, N. Kikuchi, O. Kitakami, T. Miyazaki, Y. Shimada, and K. Fukamichi, *Phys. Rev. B* **66**, 024413 (2002).
- [54] J. U. Thiele, K. R. Coffey, M. F. Toney, J. A. Hedstrom, and A. J. Kellock, *J. Appl. Phys.* **91**, 6595 (2002).
- [55] A. Sato, S. Nakagawa, and M. Takahashi, *IEEE Trans. Magn.* **36**, 2387 (2000).
- [56] A. Vansteenkiste, J. Leliaert, M. Dvornik, M. Helsen, F. Garcia-Sanchez, and B. Van Waeyenberge, *AIP Advances* **4**, 107133 (2014).
- [57] G. Bertotti, *Hysteresis in Magnetism* (Academic Press, London, 1998).
- [58] N. Honda, J. Ariake, K. Ouchi, and S. Iwasaki, *IEEE Trans. Magn.* **30**, 4023 (1994).
- [59] S. Oikawa, A. Takeo, T. Hikosaka, and Y. Tanaka, *IEEE Trans. Magn.* **36**, 2393 (2000).
- [60] Y. Inaba, T. Shimatsu, T. Oikawa, H. Sato, H. Aoi, H. Muraoka, and Y. Nakamura, *IEEE Trans. Magn.* **40**, 2486 (2004).
- [61] G. A. Bertero, D. Wachenschwanz, S. Malhotra, S. Velu, B. Bian, D. Stafford, W. Yan, T. Yamashita, and S. X. Wang, *IEEE Trans. Magn.* **38**, 1627 (2002).
- [62] H. Gong, M. Rao, D. E. Laughlin, and D. N. Lambeth, *J. Appl. Phys.* **85**, 4699 (1999).
- [63] We do not exceed the deposition temperature in order to avoid any reordering or reconstructive process different from the ones induced during the fabrication that have led to the formation of a pure hcp crystal phase.
- [64] For this particular comparison, we assume the saturation magnetization of cobalt to be $M_s = 1448 \times 10^3$ A/m, a micromagnetic exchange coupling constant $A = 1.5 \times 10^{-11}$ J m⁻¹, and a uniaxial anisotropy constant $K = 5.5 \times 10^5$ J m⁻³.
- [65] The phase boundaries that are depicted in panels (b) and (c) of Fig. 10 as solid lines are smoothed out curves based upon of the observed order parameter change that we extract from our simulations and which is discussed in the Sec. III D 3. On the other hand, the phase boundary shown as a dotted line in panels (b) and (c) of Fig. 10 is merely an approximate representation of the actual phase boundary, which can be computed by means of angular dependent calculations of the domain state energy as shown in Fig. 11.
- [66] In our micromagnetic model, we have introduced only a first-order uniaxial anisotropy energy term K for the description of the orientation dependence of the free energy. We have not considered higher-order components, which can be rather substantial in Co, but which might otherwise compromise the general applicability of our findings.